Nuclear Science and Techniques (2023) 34:31
https://doi.org/10.1007/s41365-023-01175-6

Performance of compact plastic scintillator strips with wavelength shifting fibers using a photomultiplier tube or silicon photomultiplier readout

Min Li[1,2] · Zhi-Min Wang[1,2] · Cai-Mei Liu[1,2] · Pei-Zhi Lu[3] · Guang Luo[3] · Yuen-Keung Hor[3] · Jin-Chang Liu[1,2] · Chang-Gen Yang[1,2]

Received: 13 October 2022 / Revised: 15 December 2022 / Accepted: 17 December 2022 / Published online: 3 March 2023

Abstract
This study presents the design and performance results for compact plastic scintillator strips using a wavelength shifting fiber (WLS-fiber) readout with dimensions of 0.1 m × 0.02 m × 2 m. This approach was evaluated as a candidate for a cosmic-ray muon detector for the Taishan Antineutrino Observatory (JUNO-TAO). The strips coupled with 3-inch photomultiplier tubes (PMTs) were measured and compared between the single-end and double-end readout options. Additionally, a strip using the double-end option coupling with a silicon photomultiplier (SiPM) was further evaluated and compared with the results obtained using PMTs. The performance of the strips was determined by a detailed survey along their length with a cosmic-ray muon after detailed characterization of the 3-inch PMTs and SiPMs. The proposed design employing a compact plastic scintillator strip with WLS-fiber coupling to a SiPM provides a good choice for cosmic-ray muon veto detectors, particularly when detector dimensions must be limited.

Keywords PMT · SiPM · Plastic scintillator · WLS-fiber · Muon detection · Efficiency

1 Introduction

Muon flux reaching the Earth's surface is the most abundant cosmic-ray-induced radiation at sea level [1]. Muon flux was discovered and studied by Anderson and Neddermeyer at Caltech in 1936 [2]. To tag and veto cosmic muons with high efficiency, veto systems are crucial for low background experiments, such as searching for neutrinos [3, 4], dark matter [5, 6] and double beta decay [7]. Generally, we can discriminate muons using two methods: expected energy deposition [8] with a simple energy threshold and coincidence measurements. The requirements for such a muon tag and veto system are high muon identification efficiency, gamma-ray background immunity, small detector dimension size restriction, and low unit mass cost [9, 10]. Experiments must be conducted with a limited overburden or deep underground.

The Taishan Antineutrino Observatory (JUNO-TAO) [11] is a satellite experiment of the JUNO experiment [12], a ton-level liquid scintillator (LS) detector placed ~ 30 m from the reactor core of the Taishan Nuclear Power Plant in Guangdong, China. The main purpose of TAO is to provide a reference antineutrino spectrum for JUNO to remove model dependencies in determining neutrino mass ordering, and to provide a benchmark measurement to test nuclear databases. A compact and high-efficiency muon detector is required to suppress the muon-related background. Additionally, the TAO detector location near the reactor has limited space availability, limited overburden, and higher muon flux. Following the proposal of the

This work was supported partially by the National Natural Science Foundation of China (Nos. 11875282, 11475205 and 12022505), the Strategic Priority Research Program of the Chinese Academy of Sciences (No. XDA10011200), and the Youth Innovation Promotion Association of CAS.

✉ Zhi-Min Wang
wangzhm@ihep.ac.cn

[1] Institute of High Energy Physics, Chinese Academy of Sciences, Beijing 100049, China

[2] University of Chinese Academy of Sciences, Beijing 100049, China

[3] Sun Yat-sen University, Guangzhou 510275, China

JUNO-TAO detector [11], a multi-layer detector using a plastic scintillator was proposed for muon tagging and vetoing that covers approximately 4 m ×4 m located on top of the TAO detector.

Many types of detectors have been used to detect muons. High-efficiency organic plastic scintillation (PS) detectors have been widely applied as a proven technology owing to their excellent optical transmission properties, simple production, low cost, stability, fast response time, multi-type radiation sensitivity, and excellent high radiation background performance. In many high-energy physics projects, plastic scintillator strips serve as anti-coincidence detectors to provide a trigger signal. Additionally, they are used as sensitive elements for tracking detectors, such as OPERA [13], MINOS [14], K2K SciBar detector [15], Minerva [16], TAE [17], AugerPrime [18], μCosmics [19], YBJ-HA [20], LHAASO [21, 22], muon tomography [23–25], and many other applications [26–28].

In general, the light yield (LY) [29, 30] of a scintillator and the detection efficiency are the key characteristics describing the quality of the detection setup [18]. Excellent uniformity and relatively high light collection are required to achieve high muon detection efficiency while maintaining good discrimination from gamma rays. Wavelength shifting (WLS) fibers coupled with a photomultiplier tube (PMT) or multi-pixel silicon-based avalanche photodiodes operated in Geiger mode (silicon photomultipliers (SiPMs)) are commonly used to avoid bulky light guides and read out scintillator light [31–33]. APS can be much more mechanically robust and offers great flexibility in detector size and shape, better tolerance to magnetic fields, higher photon detection efficiency, and low cost when combined with a SiPM [1, 34, 35]. Typically, the WLS fibers are placed into grooves or holes along the strip. The detection efficiency can be significantly increased by improving the optical contact between the scintillator and the fiber by adding an optical filler into the groove/hole with a high-transparency optical glue having a refractive index close to the refractive index of the strip base material (typical polystyrene). This leads to a light yield increase of up to 50% when compared to the strips without a filler [36, 37].

In this study, we proposed a basic design for PS compact strips with a WLS-fiber fiber that was 0.1 m × 0.02 m × 2 m^3, aiming for a compact muon tagging detector with good efficiency and gamma-ray identification. Prototypes employing two strips with a 1 -mm WLS-fiber were fabricated and tested. Comparisons among the readout options (single-end or double-end) and the sensor options of PMT or SiPM were performed in detail using a cosmic-ray muon survey. Section 2 will introduce the design of the strips and the testing system. Section 3 will show the results in detail. Finally, a summary is provided in Sect. 4.

2 System setup

Based on the studies and strategies discussed in Sect. 1, two kinds of PS strips with WLS-fiber were designed and produced for R &D. In this section, the strip design and the testing system are described. The photon sensors using 3-inch PMT and SiPM were also characterized.

2.1 Plastic scintillator strip with wavelength shifting fiber

The design using a compact PS strips with WLS-fiber is proposed with two readout options: single-end or double-end, as shown in Fig. 1a. The key features are the filled gaps between the scintillator and the fiber and the fiber flat surface to the PS at its end (Fig. 1b). The dimensions of the PS strip were 0.1 m × 0.02 m × 2^3 m (width × thickness × length), with four 1-mm WLS-fibers along its width direction (approximately 2-cm spacing between neighboring fibers), which were inserted and glued by a filler into the grooves on the PS surface. The four fibers of the double-end option were gathered into two groups at each end (four groups in total) and coupled to the photon sensors. There were only two groups at the output end of the single-end option (no fiber cut at the other end) that aimed to reduce the sensor and electronics channels.

The prototypes of the designed PS strips were finalized and fabricated by *Beijing Hoton Nuclear Technology Co., Ltd.* [38]. The two strips were made with an extruded SP101 plastic scintillator polymerized with liquid polystyrene containing P-triphenyl and POPOP. The groove was 6 mm × 6 mm in an optical window of 1 cm × 4 cm, as shown in Fig. 1b, where the WLS-fiber BCF92 [39] had a 1-mm diameter and its end surface was flat. The PS strip was first covered with a 0.08-mm Al film, then another 0.8-mm PVC layer, and finally packaged with a black adhesive tape layer. The scintillation photons were collected through the WLS-fiber and read out by photon sensors, such as SiPMs or PMTs, which were measured and compared. This is described in detail and discussed in the following sections.

2.2 Electronics and data acquisition (DAQ)

A general schema of the testing system is shown in Fig. 2. Two small PS modules (mini-modules PS1 and PS2) were located above and below the PS strip, respectively (Fig. 3b), used for muon tagging. The signals of the 2-inch PMTs on the PS mini-modules were sent to a FIFO module (OCTAL LINEAR model 748) and then discriminated by a low-threshold discriminator (CERN N845). The coincidence (CAEN logic module N455) was

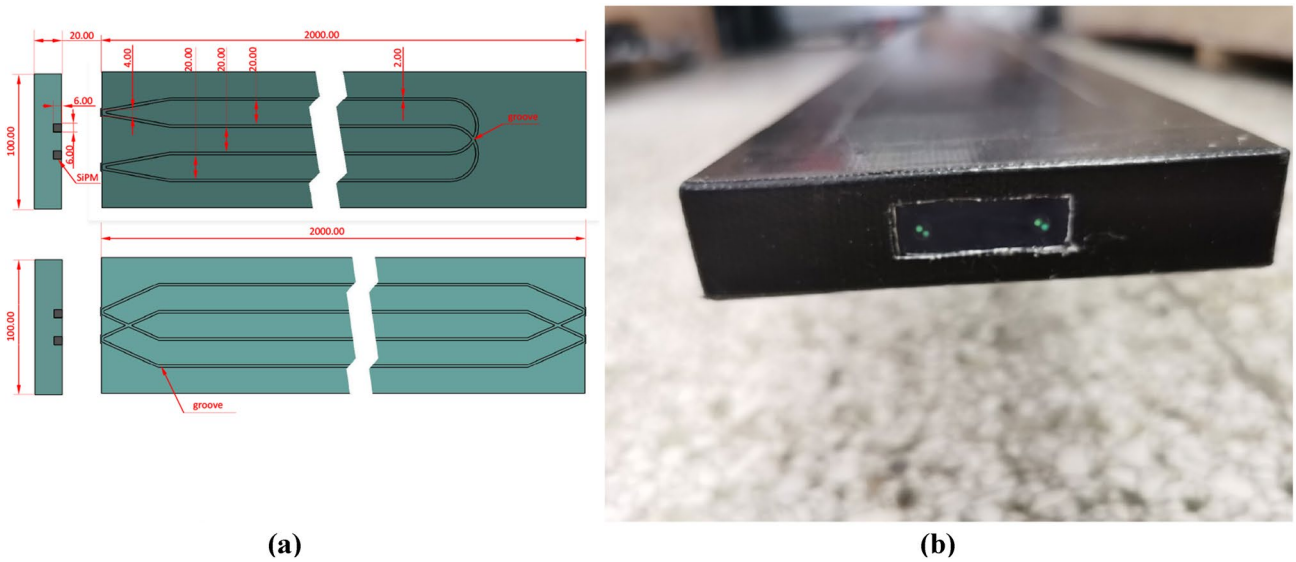

Fig. 1 (Color online) Design of the compact PS strip and the flat surface of the fibers to the PS at its end. **a** Design of PS with WLS-fiber; **b** Gathered fibers and optical window

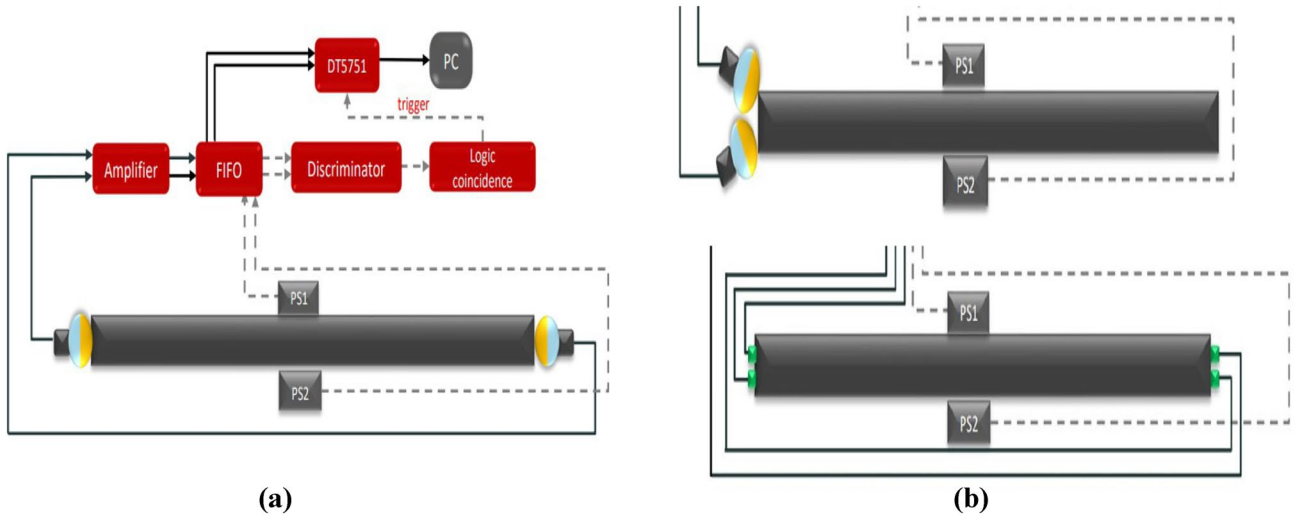

Fig. 2 (Color online) Schema of system setup. The mini-modules (PS1 and PS2) surveyed nine locations of the PS strip with 0.2-m step between −0.8 m (minimum −1 m, left end, side A) and 0.8 m (maximum 1 m, right end, side B). **a** Double-end setup with SPMTs; **b** Single-end SPMTs and double-end SiPMs

used to tag a muon as a trigger for the data acquisition (DAQ) system. The mini-modules were surveyed along the length of the PS strip to check uniformity, which was used for all the following tests: single-end, double-end, PMT, and SiPM. Two 3-inch PMTs (SPMT) or four SiPMs were used to collect photons, where the SiPMs (SPMTs) were directly coupled to the PS strip through the air (Fig. 3a). Please note that two 3-inch SPMTs were used for both single-end and double-end options: one SPMT for each end covered two fiber groups of the double-end option, while one of the two SPMTs in single-end covered only one fiber group of the single-end option (Fig. 2b). Each of the four SiPMs covered one of the four fiber groups of the double-end option (Fig. 2b). All sensor signals were first sent to the FIFO and then recorded in waveforms by an FADC (CAEN DT5751, 1 GS/s, 1 V p-p) triggered by the mini-modules. Each SiPM had its own individual high-voltage (HV) power supply, and an additional amplifier was applied to SiPM4 to improve its signal-to-noise ratio, as discussed later.

Fig. 3 (Color online) Experimental setup. **a** The style of coupling; **b** Trigger

2.3 Mini-modules for muon trigger

Two mini-modules (PS1, 25 cm × 4 cm × 30 cm and PS2, 15 cm × 1 cm × 22 cm), equipped with a 2-inch PMT, were used to tag muons and calibrate the performance of the designed PS strips. The measured spectra of the mini-modules in terms of amplitude and charge are shown in Fig. 4, where the 2-inch PMTs were set to −2200 V (PS1) and −1800 V (PS2) for a similar operating gain, respectively. The threshold of the mini-modules in amplitude was set to approximately 10 mV (PS1) and 2 mV (PS2) (Fig. 4a to select muons. The threshold value difference is mainly due to their light yield related to their thickness, which introduced different valley locations in their charge spectra, as shown in Fig. 4b. The coincidence rate of the two mini-modules was approximately 6–7 Hz including muons, background, and possible random coincidence.

2.4 Three-inch photomultiplier tube (SPMT) and silicon photomultiplier (SiPM)

The PS strips were coupled with SiPMs and SPMTs to collect photons at room temperature (25 °C). Four SiPM pieces were used in this study, including three HPK S14160 with dimensions of 3 mm × 3 mm [40] (SiPM1, SiPM2, SiPM3), which is favored for its relatively low HV, high gain, good photon detection efficiency, lower noise, and smaller cross talk. Coincidentally, the other SiPM type, S12572, was also tested as a backup and comparison. Three-inch PMTs (SPMT) from HZC [41] were used as a reference for comparison with the SiPMs because they have good stability and low noise for single- and double-end options. The characterization of the SiPM was performed first with a procedure similar to that in [42], but mainly focused on its gain versus over-voltage

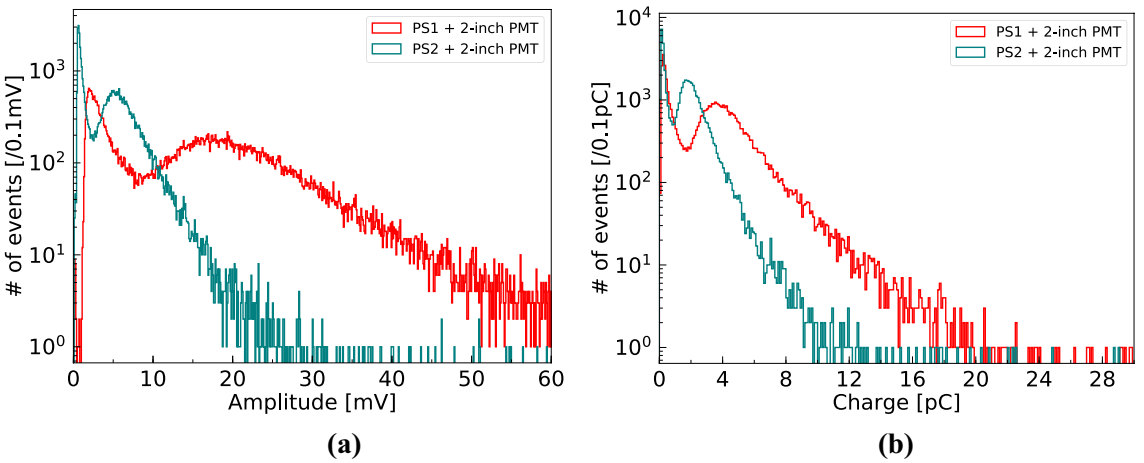

Fig. 4 (Color online) Amplitude and charge spectra of the mini-modules. **a** Amplitude; **b** Charge

(OV) by light-emitting diode (LED), cross-talk (CT), and dark count rate (DCR).

The SiPM measurements are shown in Fig. 5, where the typical charge spectra measured with SiPM3 and SiPM4 are shown in Fig. 5a, and the working gain of the SiPMs was calculated according to the peaks. The relationship between the gain and OV is plotted in Fig. 5b, where the breakdown voltage (V_{bd}) was estimated by curve fitting the gain versus applied voltage. The breakdown voltage was approximately 41 V for SiPM1–3 and 71 V for SiPM4. An OV of 3 V was set for all the SiPMs. The SiPM used another fast ×10 amplifier owing to its low gain. A typical plot of DCR versus the SiPM amplitude threshold is shown in Fig. 5c, where the DCR was decreased in steps by increasing the threshold. The DCR was approximately 500 kHz at a half photoelectron (p.e.) equivalent threshold of 55 kHz/mm^2). The measured CT ratio was approximately 12% for SiPM1–3 and 46% for SiPM4. The high cross-talk ratio of the SiPMs, as shown in Fig. 5d, affected its charge measurement. A decreasing factor of 1/8 was applied to estimate the DCR for every other p.e. threshold increase. The DCR and CT also affected the threshold setting, muon efficiency, and random coincidence expectation of the PS strip.

The gains of the two used SPMTs were calibrated and tuned to 3×10^6 with a positive HV of 1150 V and 1180 V, respectively. The quantum efficient (QE) of the SPMTs was approximately 23%, and the DCR was approximately 400–700 Hz at a single p.e. threshold (~2.5 mV/p. e.), which was much smaller than that of the SiPMs. The measured charge of a single photoelectron (SPE) and the DCR versus threshold are shown in Fig. 6.

3 Results and discussion

Using the system introduced in Sect. 2, the measurements and comparisons were implemented for coupling with a SiPM and PMT, and single- and double-end options of the PS strips, respectively. The muon efficiency of the PS strips was measured and calculated at nine locations along its longitudinal direction. Based on the measured charge and hit-time spectra of the PS strip triggered by the coincidence

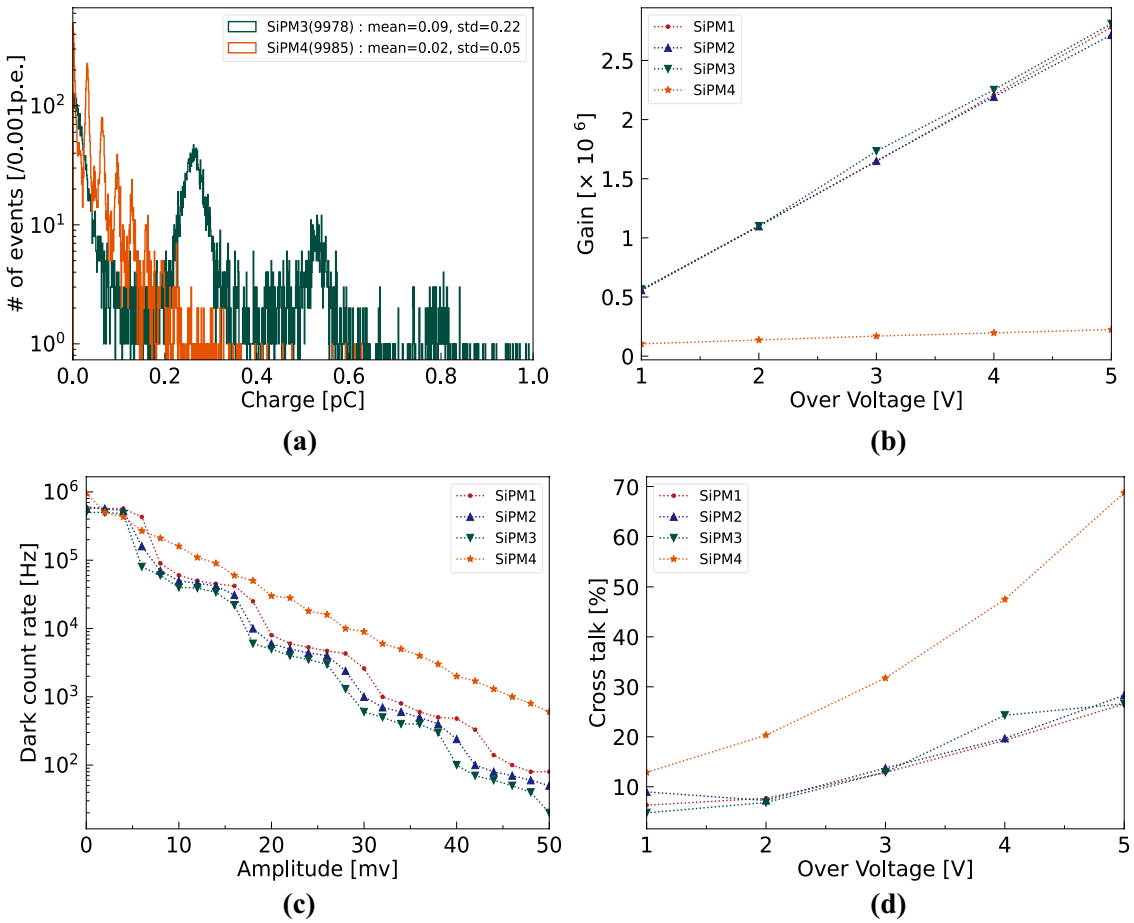

Fig. 5 (Color online) Measured spectra of the SiPMs. **a** Charge spectra of SiPMs; **b** Gain versus OV; **c** DCR versus amplitude; **d** CT versus OV

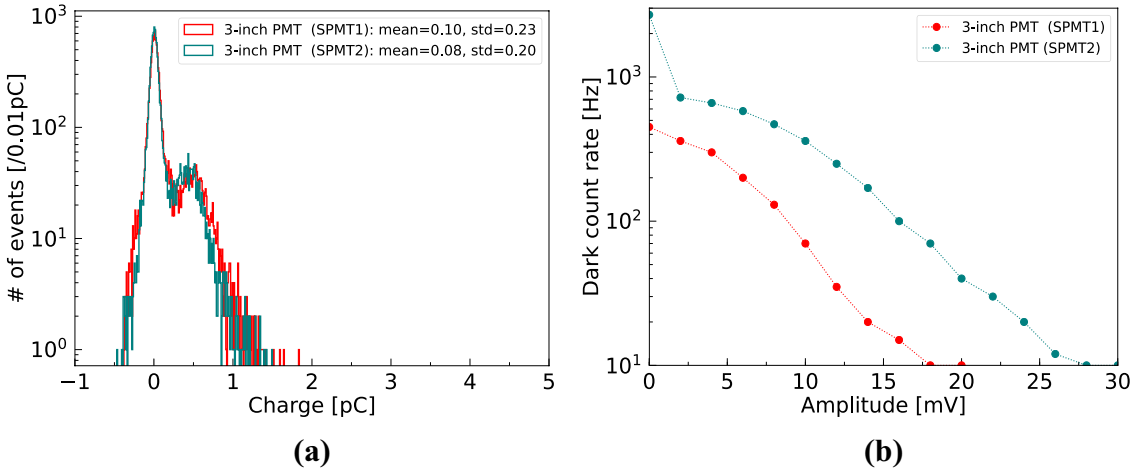

Fig. 6 (Color online) Measured SPE charge spectrum and the DCR versus amplitude of the SPMTs. **a** SPE charge spectrum; **b** DCR versus amplitude threshold

of the mini-modules, as shown in Fig. 7, further cuts on hit-time and charge were used to remove the random noise coincidence and select more pure muon samples hitting the PS strip. For example, hit-time in the range of [390,420] ns for SPMTs ([320,360] ns for SiPMs) and charge higher than 0.4 p.e. were used for the following analysis. According to the measured charge spectrum, the systematic bias of the calculated muon efficiency was estimated to be less than 0.5% from an applied charge threshold of 0.4 p.e.

3.1 Plastic scintillator strip with SPMT

The PS strips coupled with SPMTs were first measured as a reference, where the optical window of each fiber group was further reduced to a dimension of 5 mm × 5 mm. The two fiber groups at one end (side A or side B) of the double-end PS strip were covered by a single SPMT, and each fiber group of the single-end PS strip was covered by a single SPMT where no coupling gel was used between the PS and SPMT. The charge spectra in p.e. measured by the SPMTs (sum of the two SPMTs) are plotted for both the single-end and double-end options with a threshold of 0.4 p.e., as shown in Fig. 8a for the single-end option and Fig. 8b for the double-end option.

The light yield (LY) at each location was defined as the mean value of the measured charge spectrum. The LY value of the single-end option (Fig. 8c) exhibited monotonous decline when the muon hitting location was sufficiently far from the readout end (−1 m, SPMTs). By contrast, the minimum LY of the double-end option with a

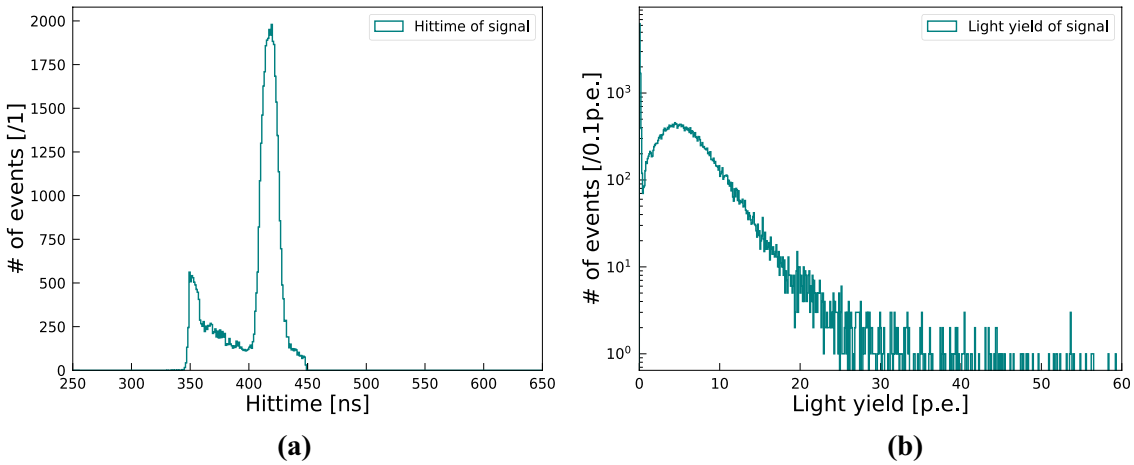

Fig. 7 PMT charge and hit-time distribution of the PS strip with the coincidence trigger of the mini-modules. **a** PMT hit-time of PS; **b** PMT light yield of PS

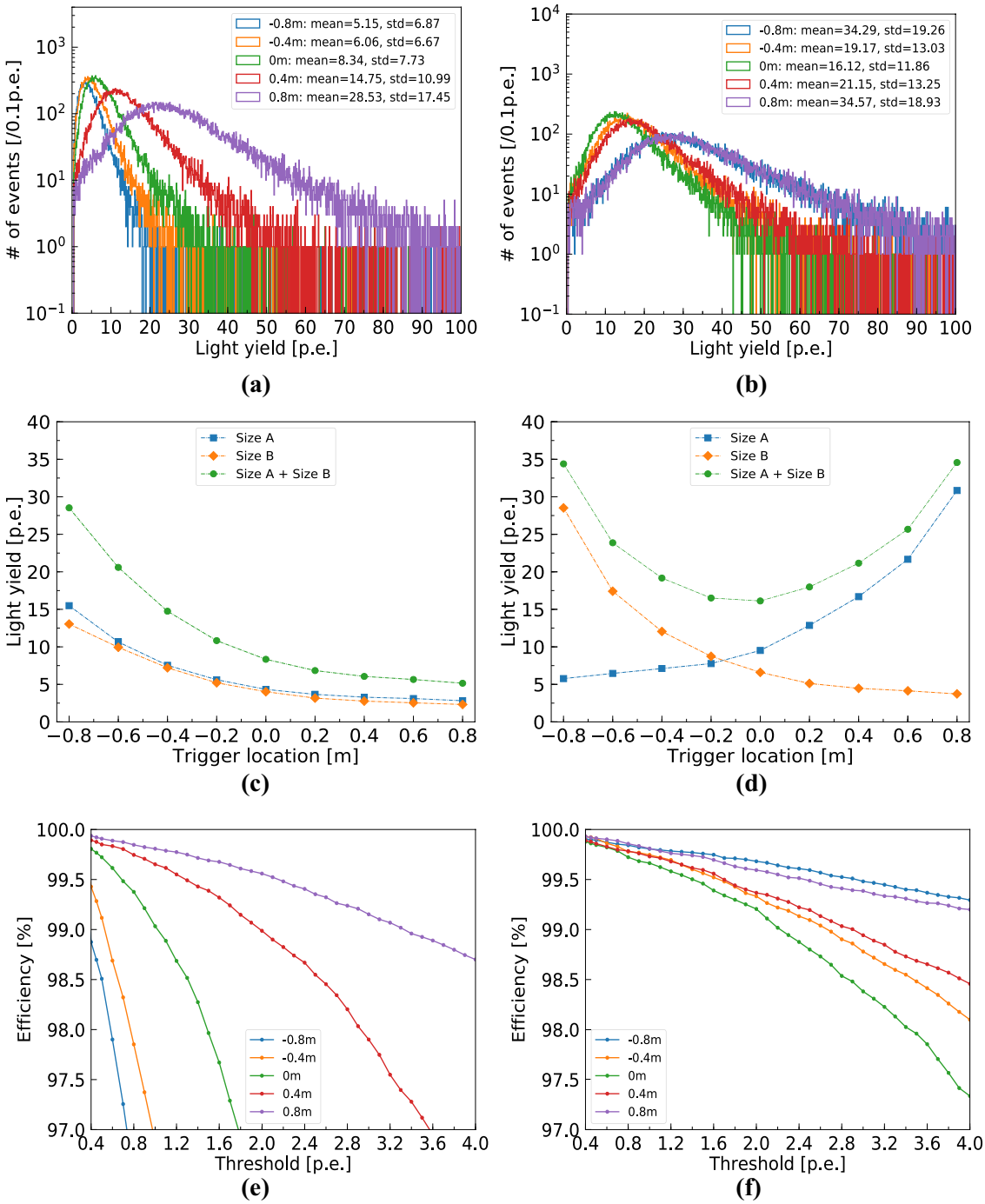

Fig. 8 (Color online) Measured spectra of the measured charge spectra (top), light yield versus locations (middle), and muon efficiency versus locations (bottom) of the PS modules coupled with PMTs for single-end (left) and double-end (right) options, respectively. **a** Charge spectra of single-end; **b** Charge spectra of double-end; **c** LY versus location of single-end; **d** LY versus location of double-end; **e** Muon efficiency versus threshold of single-end; **f** Muon efficiency versus threshold of double-end

symmetrical shape (Fig. 8d) was at the middle of the strip, as expected, because of the attenuation length of the fibers and the solid angle of PS flashing point to the PMTs. The LY of the single-end option was slightly larger than that of the double-end option, which was the main source of the additional light returning from the far end of the fibers.

The muon tagging efficiency of the PS strips is defined as the ratio between the coincidence event number of the

two SPMTs over the threshold to the event number in total triggered by the mini-modules and selected by hit time and charge, as shown in Fig. 7a, b. The calculated results are shown in Fig. 8e for the single-end option and Fig. 8f for the double-end option, respectively. With a threshold lower than 2.0 p.e., the double-end option can achieve an efficiency higher than 99% for all locations, but the single-end option needs to lower the threshold to approximately 0.5 p.e. The efficiency was much worse for at least half of the locations with a threshold of 0.5–1 p.e. as well. The muon efficiency increased similarly to the double-end option if we summed the signals of the two SPMTs as a single channel of the single-end option, instead of the currently used coincidence of the two SPMTs. It is feasible for option coupling with the PMT, but it would introduce a higher noise from DCR without coincidence suppression for SiPMs, in particular.

According to the results, the double-end option was preferred over the single-end option for better LY and tolerance of threshold versus efficiency. This is especially true for coupling with SiPMs to suppress the higher DCR in the range of 1–3 p.e. The measured muon rate of the double-end PS strip coupled with SPMTs can be estimated with a threshold of approximately 10 p.e. on the total light intensity (~4 p.e. of each end) to reach around 95% muon efficiency (Fig. 8f) without further coincidence between strips.

3.2 Plastic scintillator (PS) strip with silicon photomultiplier (SiPM)

The PS strip with WLS-fiber and the double-end option coupled with SiPMs is evaluated in this section. The optical window for each fiber group was 5 mm × 5 mm. Each of the optical windows was partially covered by a single SiPM cell with dimensions of 3 mm × 3 mm centered on the fiber, where no coupling gel was used between the PS and SiPMs. The summed spectra of the four SiPMs for the double-end option are shown in Fig. 9a. The LY versus the measurement location is shown in Fig. 9b, which shows a similar trend as the PS strip with SPMTs (Fig. 8d). The higher LY than that with PMTs was mainly from the QE difference and SiPM cross-talk. The LY inconsistencies of sides A and B were further verified for each SiPM, as shown in Fig. 9c for side A and in Fig. 9d for side B. Both SiPMs in one end (SiPM1 and SiPM2, or SiPM3 and SiPM4) showed a consistent trend, except for the point at 0.8 m of SiPM3. The difference in values was possibly from the coupling status between the PS and SiPM, the PS strip itself, and the QE of SiPMs, which still require careful validation.

The muon efficiency versus location was also derived. An example of muon efficiency with different trigger conditions at location 0 m is shown in Fig. 9e, where the efficiency of side A (also side B) was calculated only with the coincidence of SiPM1 and SiPM2 over the threshold, and the efficiency of together side A and side B was from the coincidence of side A over a threshold (sum of SiPM1 and SiPM2) and side B over a threshold (sum of SiPM3 and SiPM4). Compared to the single-end option with SPMTs as, shown in Fig. 8e, the threshold could reach approximately 2–3 p.e. for higher than 99% efficiency, but the random coincidence of the SiPM DCR and the cross-talk still could not be ignored. The efficiency of sides A and B was considerably better than that of the single-end, as expected and discussed for coupling with the SPMT. The muon efficiency of side A and side B combined is shown in Fig. 9f, and it can reach the required 99% efficiency even with the threshold rising to around 4 p.e. This is much improved over the PS with PMTs because of the better light yield of SiPMs, even if it has higher coupling challenges.

Considering the threshold tolerance to the required 99% muon efficiency, the double-end option coupled with four SiPMs is preferred, which is a good choice even if there are imperfect or unexpected issues with the PS strip, coupling, etc. A threshold of approximately 15 p.e. on the sum light intensity of the double-end option coupled with four SiPMs (~7 p.e. threshold of side A or side B) can be used to identify muons with an efficiency of approximately 98–99% without further coincidence.

3.3 Comparison of plastic scintillators (PS) with three-inch photomultiplier tube (SPMT) and silicon photomultiplier (SiPM)

A direct comparison between the PS strips of the single-end and double-end options is shown in Fig. 10, where the double-end option shows a higher light yield (Fig. 10a) and better muon efficiency (Fig. 10b) under the same threshold for both couplings with an SPMT and SiPM. The option coupled with an SiPM has the highest LY compared to the other two options, even at approximately 0.8 m (near the end of side B), where the SiPMs or the coupling experienced challenges. The efficiency of the option coupled with an SiPM under the same threshold was also higher than that of the other two options.

Evaluating the readout options between the PMT and SiPM in double-end mode, the SiPM exhibited higher light yield, efficiency, and reachable threshold. The SiPM can also minimize the occupied dimensions for a similar active volume, as designed. The higher random coincidence rate resulting from the SiPM DCR can be suppressed by the coincidence of sides A and B or by increasing the threshold (55 kHz/mm^2, 100 ns coincidence window, 12% cross-talk, (SiPM1 or SiPM2) and (SiPM3 or SiPM4)): ~98 kHz at threshold 0.5 p.e., ~1.5 kHz at threshold 1.5 p.e., ~24 Hz at threshold 2.5 p.e., and ~0.37 Hz at threshold 3.5 p.e. The temperature effect of the SiPM can also be minimized by a high LY and reachable threshold.

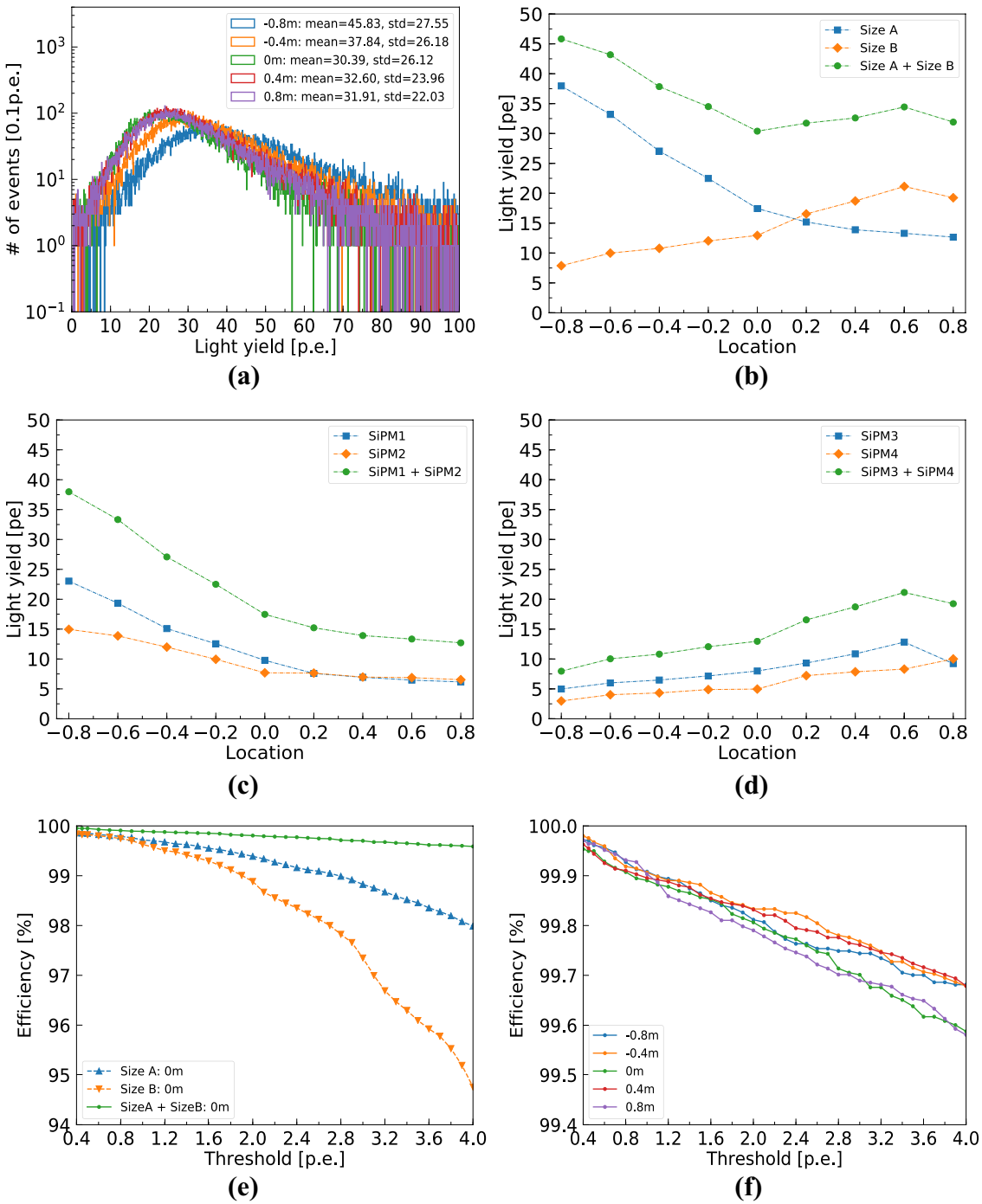

Fig. 9 (Color online) Measured charge spectra (top left), light yield in sum versus locations (top right), light yield of side A (middle left), light yield of side B (middle right), muon efficiency of location 0 m with different trigger modes (bottom left), and muon efficiency versus different locations with side A and side B triggers(bottom right), respectively. **a** Summed charge spectra; **b** LY versus location; **c** LY versus location by side A; **d** LY versus location by side B; **e** Muon efficiency of trigger mode versus threshold (0 m); **f** Muon efficiency versus threshold along the PS

A comparison of the charge spectra directly measured by the PS strip of the double-end option coupled with SPMT and SiPM is shown in Fig. 11a. The y-axis is normalized to the muon event of the coupling to an SiPM or SPMT and the measured rate between the coupling of the SiPM and SPMT. The threshold was 0.25 p.e., 0.5 p.e., 0.75 p.e., and 1.0 p.e. for each SPMT with a coincidence of sides A and B, and 1.0 p.e., 2.0 p.e., 3.0 p.e., and 4.0 p.e. for each SiPM

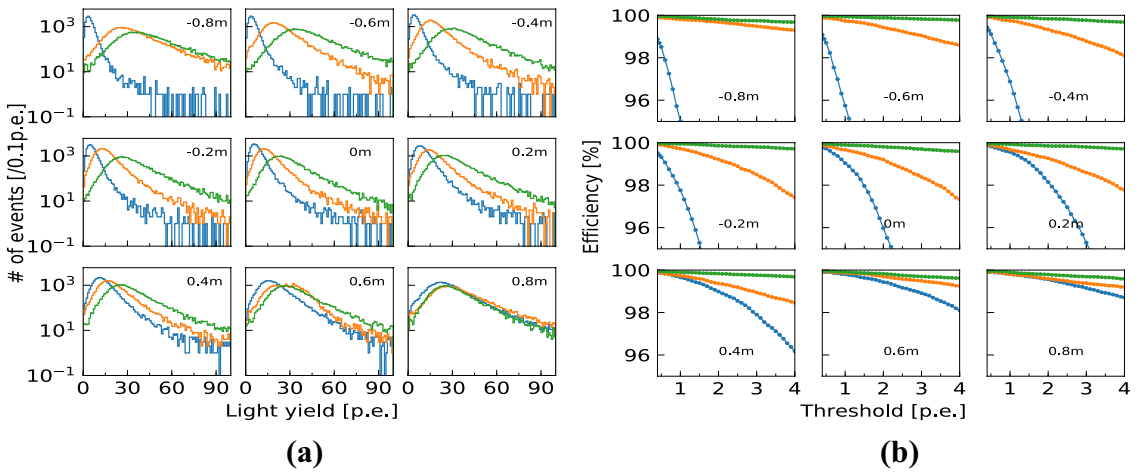

Fig. 10 (Color online) Comparison of light yield and muon efficiency of PS strips with SiPMs and PMTs. Green double-end (SiPM), orange double-end (SPMT), and blue single-end (SPMT). **a** Comparison of LY and PS; **b** Comparison of efficiency and PS

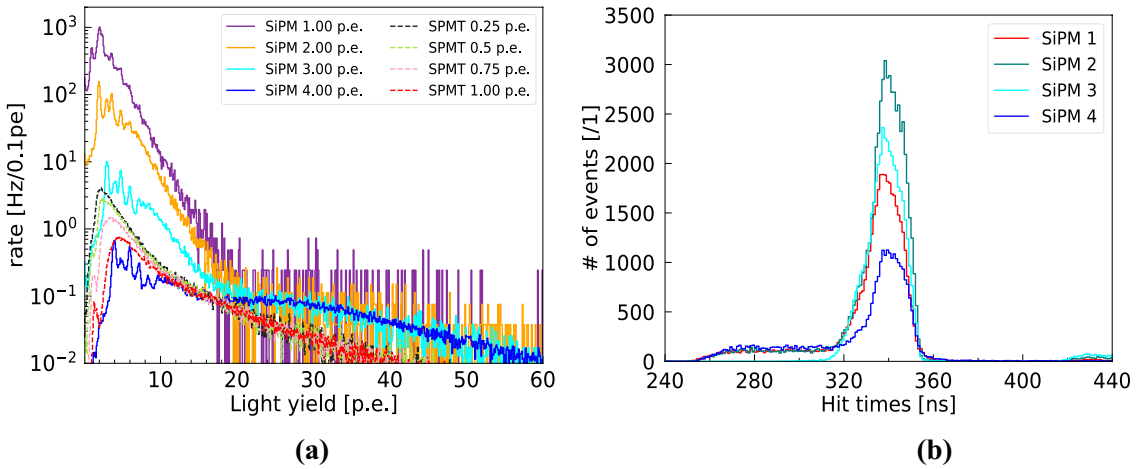

Fig. 11 (Color online) Comparison of light yield and muon efficiency of PS strips with SiPMs and PMTs. Green double-end (SiPM), orange double-end (SPMT), and blue single-end (SPMT). **a** Comparison of LY and PS; **b** Comparison of efficiency and PS

with a coincidence of SiPM1 and SiPM2 (side A) or SiPM3 and SiPM4 (side B), which is not the coincidence of side A (sum of SiPM1 and SiPM2) and side B (sum of SiPM3 and SiPM4) limited by the hardware. The expected muon efficiency for all configurations was higher than 98–99%.

The measured rate of the strip coupled with SPMTs was ~160 Hz, ~120 Hz, ~80 Hz, and ~50 Hz with each threshold setting as listed, respectively, which were mainly from natural radioactivity and cosmic-muon (approximately 20 Hz under a muon rate of 100 Hz/m^2 at sea level). The random coincidence of the SPMT DCR was less than 0.1 Hz, approximately 20 Hz higher than the 10 p.e. threshold of a muon to the sum of sides A and B, and the relative contribution of the radioactivity was approximately 140 Hz for the 0.25 p.e. threshold. The measured rate of the strip coupled with SiPMs was ~30,000 Hz, ~4,500 Hz, ~320 Hz, and ~50 Hz for each threshold setting, as shown in Table 1, respectively, approximately 20 Hz higher than the

Table 1 Coincidence rate of the double-end strip coupled with SPMT and SiPM with different thresholds

Threshold (p.e.)				
SPMT	0.25	0.5	0.75	1.0
SiPM	1.0	2.0	3.0	4.0
SPMT rate (Hz)	~160	~120	~80	~50
SiPM rate (Hz)	~30,000	~4,500	~320	~50
SiPM random Coincidence rate (Hz)	>10,730	>2,280	>180	>15

15 p.e. threshold for muon selection to the charge sum of sides A and B.

The measured rate of the PS strip coupled with an SiPM was considerably higher than that coupled with SPMT, particularly the lower threshold, which was partially from the radioactivity with a higher LY and mainly by the random coincidence of DCR. Many events were located in the region where it is lower than the required sum light intensity of all SiPMs over the threshold, including lower than 2 p.e. of 1 p.e. threshold, lower than 4 p.e. of 2 p.e. threshold, lower than 6 p.e. of 3 p.e. threshold, and lower than 8 p.e. of 4 p.e. threshold. This is because of the required hit-time region in [320, 360] ns as the SiPM analysis window, considering the difference in muon hit-time. However, it is 100 ns of the coincidence window for two SiPMs of sides A and B for the data acquisition trigger, where the random coincidence of the SiPM DCR contributed significantly, as shown in Fig. 11b. In this case, only one of the hits inside the analysis window were from the SiPM DCR, while the others outside of the analysis window were ignored. The hits outside the window were considered for the summed light intensity calculation and contributed to the region that was higher than the threshold of a single SiPM, but lower than the sum of their coincidence. Moreover, we calculated the random coincidence rate from the SiPM DCR within this region of the summed light intensity spectra, which was correlated and proportional to the real random coincidence. The calculated random coincidence rate was approximately ~ 10,730 Hz, ~2,280 Hz, ~180 Hz, and ~15 Hz for each SiPM threshold setting (Table 1), which is consistent with the previous calculation.

4 Summary

In this study, a compact design of a plastic scintillator with WLS-fiber was proposed, fabricated, and measured. The options were compared between single-end and double-end coupling with PMT or SiPM. The results demonstrated that the double-end option is preferred for JUNO-TAO, considering the light yield and muon efficiency. The option coupled with an SiPM achieved a better performance along a 2-m plastic scintillator and exhibited better tolerance to noise and threshold, even though the coupling of one side faced challenges. (The coupling between PS and SiPM can be improved further.) The proposed option with an SiPM is suitable for a compact requirement, appreciable light yield (minimum ~30 p.e./muon), and robustness. This offers a quantitative candidate for a scintillator/WLS-fiber configuration for future muon tagging detectors. Furthermore, the results can also be used for other general designs of scintillator-based detectors with a WLS-fiber read-out.

Author Contributions All authors contributed to the study conception and design. Material preparation, data collection, and analysis were performed by Min Li, Zhi-Min Wang, and Cai-Mei Liu. The first draft of the manuscript was written by Min Li and Zhi-Min Wang, and all authors commented on previous versions of the manuscript. All authors read and approved the final manuscript.

References

1. C. Liao, H. Yang, Z. Liu et al., Design and characterization of a scintillator-based position-sensitive detector for muon imaging. Nucl. Technol. **205**, 736–747 (2019). https://doi.org/10.1080/00295450.2018.1522885
2. C.D. Anderson, S.H. Neddermeyer, Cloud chamber observations of cosmic rays at 4300 meters elevation and near sea-level. Phys. Rev. **50**, 263 (1936). https://doi.org/10.1103/PhysRev.50.263
3. A. Abusleme, T. Adam, S. Ahmadet et al., JUNO physics and detector. Prog. Part. Nucl. Phys. **123**, 103927 (2022). https://doi.org/10.1016/j.ppnp.2021.103927
4. J. Ashenfelter, A.B. Balantekin, C. Baldenegro et al., The prospect reactor antineutrino experiment. Nucl. Instrum. Meth. A **922**, 287–309 (2019). https://doi.org/10.1016/j.nima.2018.12.079
5. P. Agnes, T. Alexander, A. Alton et al., Direct search for dark matter with DarkSide. J. Phys. Conf. Ser. **650**, 012006 (2015). https://doi.org/10.1088/1742-6596/650/1/012006
6. H. Zhang, A. Abdukerim, W. Chen et al., Dark matter direct search sensitivity of the PandaX-4T experiment. Sci. China Phys. Mech. Astron. **62**, 31011 (2015). https://doi.org/10.1007/s11433-018-9259-0
7. N. Ackerman, B. Aharmim, M. Auger et al., Observation of two-neutrino double-beta decay in Xe-136 with EXO-200. Phys. Rev. Lett. **107**, 212501 (2011). https://doi.org/10.1103/PhysRevLett.107.212501
8. Z.Y. Li, Z. Qian, J.H. He et al., Improvement of machine learning-based vertex reconstruction for large liquid scintillator detectors with multiple types of PMTs. Nucl. Sci. Tech. **33**, 93 (2022). https://doi.org/10.1007/s41365-022-01078-y
9. G. Giannini, G. Santin, M. Spinetti et al., Plastic scintillator bar with WLS fiber calorimeter for neutrino physics. Nucl. Instrum. Math. A **461**, 316–318 (2001). https://doi.org/10.1016/S0168-9002(00)01231-6
10. C.F. Yang, Y.B. Huang, J.L. Xu et al., Reconstruction of a muon bundle in the JUNO central detector. Nucl. Sci. Tech. **33**, 59 (2022). https://doi.org/10.1007/s41365-022-01049-3
11. A. Abusleme, T. Adam, S. Ahmad et al., TAO conceptual design report: a precision measurement of the reactor antineutrino spectrum with sub-percent energy resolution. https://doi.org/10.48550/arXiv.2005.08745
12. F.P. An, G.P. An, Q. An et al., Neutrino physics with JUNO. J. Phys. G **43**, 0030401 (2016). https://10.1088/0954-3899/43/3/030401
13. E. Baussan, K. Borer, J.E. Campagne et al., The neutrino oscillation OPERA experiment target tracker. Nucl. Instrum. Nucl. Instrum. Meth. A **581**, 465–468 (2007). https://doi.org/10.1016/j.nima.2007.08.028
14. P. Adamson, K. Alexandrov, G. Alexeev et al., The MINOS scintillator calorimeter system. IEEE Trans. Nucl. Sci. **581**, 861–863 (2007). https://doi.org/10.1109/TNS.2002.1039579
15. K. Nitta, E. Aliu, S. Andringa et al., The K2K SciBar detector. Nucl. Instrum. Meth. A **535**, 147–151 (2004). https://doi.org/10.1016/j.nima.2004.07.272
16. H.S. Budd, The design and performance of the MINERνA experiment. Phys. Procedia **37**, 1311–1318 (2012). https://doi.org/10.1016/j.phpro.2012.02.475

17. Y. Tameda, the Telescope Array Experiment, Telescope array experiment. Nucl. Phys. B-Pro. Sup. **196**, 74–79 (2009). https://doi.org/10.1016/j.nuclphysbps.2009.09.011
18. Z.Z. Zong, G. Hull, M. Imre et al., Study of light yield for different configurations of plastic scintillators and wavelength shifting fibers. Nucl. Instrum. Meth. A **908**, 82–90 (2018). https://doi.org/10.1016/j.nima.2018.08.029
19. A.G. Tsirigotis, A. Leisos, μCosmics: ANBA low-cost educational cosmic ray telescope. Universe **5**, 23 (2019). https://doi.org/10.3390/universe5010023
20. Z. Wang, Y.Q. Guo, H. Cai et al., Performance of a scintillation detector array operated with LHAASO-KM2A electronics. Exp. Astron. **45**, 363–377 (2018). https://doi.org/10.1007/s10686-018-9588-z
21. Y.P. Wang, C. Hou, X.D. Sheng et al., Testing and analysis of the plastic scintillator units for LHAASO-ED. Radiat. Detect. Technol. Methods **5**, 513–519 (2021). https://doi.org/10.1007/s41605-021-00274-5
22. F. Aharonian, Q. An, F. Axikegu et al., Performance test of the electromagnetic particle detectors for the LHAASO experiment. Nucl. Instrum. Meth. A **1001**, 165193 (2021). https://doi.org/10.1016/j.nima.2021.165193
23. F. Nishikido, T. Moritake et al., X-ray detector made of plastic scintillators and WLS fiber for real-time dose distribution monitoring in interventional radiology. Symp. Conf. Rec. IEEE Nucl. Sci. (2012). https://doi.org/10.1109/NSSMIC.2012.6551311
24. C. Park, M.K. Baek, I. Kang et al., Design and characterization of a Muon tomography system for spent nuclear fuel monitoring. Nucl. Eng. Technol. **54**, 601–607 (2022). https://doi.org/10.1016/j.net.2021.08.029
25. J.N. Dong, Y.L. Zhang, Z.Y. Zhang et al., Position-sensitive plastic scintillator detector with WLS-fiber readout. Nucl. Sci. Tech. **29**, 117 (2018). https://doi.org/10.1007/s41365-018-0449-2
26. U. Bravar, P.J. Bruillard, E.O. Flckiger et al., Design and testing of a position-sensitive plastic scintillator detector for fast neutron imaging. IEEE Trans. Nucl. Sci. **53**, 3894–3903 (2006). https://doi.org/10.1109/TNS.2006.886046
27. Y. Yang, C.P. Yang, J. Xin et al., Performance of a plastic scintillation fiber dosimeter based on different photoelectric devices. Nucl. Sci. Tech. **32**, 120 (2021). https://doi.org/10.1007/s41365-021-00965-0
28. J. Hou, Y.F. Qi, H.Y. Luan et al., Optimisation and performance test of fibre-based large-area surface contamination monitor. Results Phys. **15**, 102727 (2019). https://doi.org/10.1016/j.rinp.2019.102727
29. V. Senchyshyn, B. Grynyov, S. Melnychuk et al., Influence of polystyrene scintillator strip methods of production on their main characteristics. Radiat. Meas. **42**, 911–914 (2007). https://doi.org/10.1016/j.radmeas.2007.02.051
30. P.D. Anna, D.A. Bross, M.L. Kerry et al., Low-cost extruded plastic scintillator. Nucl. Instrum. Meth. A **466**, 482–491 (2001). https://doi.org/10.1016/S0168-9002(01)00177-2
31. W. Bugg, Yu. Efremenko, S. Vasilyev, Large plastic scintillator panels with WLS fiber readout: Optimization of components. Nucl. Instrum. Meth. A **758**, 91–96 (2014). https://doi.org/10.1016/j.nima.2014.05.055
32. J.W. Seo, E.J. Jeon, W.T. Kim et al., A feasibility study of extruded plastic scintillator embedding WLS fiber for AMoRE-II muon veto. Nucl. Instrum. Meth. A **1039**, 167123 (2022). https://doi.org/10.1016/j.nima.2022.167123
33. O. Mineev, Y. Kudenko, Y. Musienko et al., Scintillator detectors with long WLS fibers and multi-pixel photodiodes. J. Instrum. **6**, P12004 (2011). https://doi.org/10.1088/1748-0221/6/12/P12004
34. E. Garutti, Silicon photomultipliers for high energy physics detectors. J. Instrum. **6**, C10003 (2011). https://doi.org/10.1088/1748-0221/6/10/c10003
35. A. Papa, G. Cavoto, E. Ripiccini et al., A simulation tool for scintillating fibers coupled to SIPM for MIP and heavy ionizing particle identification. J. Instrum. **9**, C05066 (2014). https://doi.org/10.1088/1748-0221/9/05/C05066
36. B. Barton, D. Mills, A high-efficiency cosmic ray veto detector for the Mu2e experiment. NuFACT **21**, 452 (2018). https://doi.org/10.22323/1.341.0034
37. A. Artikov, V. Baranov, J. Budagov, Light yield and radiation hardness studies of scintillator strips with a filler. Nucl. Instrum. Meth. A **930**, 87–94 (2019). https://doi.org/10.1016/j.nima.2019.03.087
38. Hoton Technology Co. Beijing Hoton Nuclear Technology Co Ltd., (2014)
39. Saint-Gobain Group. SAINT-GOBAIN CRYSTALS, (2021)
40. Hamamatsu Photonics K.K. S14160-3050HS, 2002
41. C.Y. Cao, J.L. Xu, M. He et al., Mass production and characterization of 3-inch PMTs for the JUNO experiment. Nucl. Instrum. Meth. A **1005**, 165347 (2021). https://doi.org/10.1016/j.nima.2021.165347
42. R. Klanner, Characterisation of SiPMs. Nucl. Instrum. Meth. A **926**, 36–56 (2019). https://doi.org/10.1016/j.nima.2018.11.083